Journal of Power Sources 195 (2010) 1726–1730

Contents lists available at ScienceDirect

Journal of Power Sources

journal homepage: www.elsevier.com/locate/jpowsour

Short communication

Comparison of electrochemical performance of as-cast Pb–1 wt.% Sn and Pb–1 wt.% Sb alloys for lead-acid battery components

Wislei R. Osório*, Leandro C. Peixoto, Amauri Garcia

Department of Materials Engineering, University of Campinas – UNICAMP, PO Box 612, 13083–970 Campinas, SP, Brazil

ARTICLE INFO

Article history:
Received 14 September 2009
Accepted 30 September 2009
Available online 7 October 2009

Keywords:
Lead–tin and lead–antimony alloys
Lead-acid battery
Cellular morphology
Electrochemical impedance
Corrosion behavior

ABSTRACT

A comparative experimental study of the electrochemical features of as-cast Pb–1 wt.% Sn and Pb–1 wt.% Sb alloys is carried out with a view to applications in the manufacture of lead-acid battery components. The as-cast samples are obtained using a water-cooled unidirectional solidification system. Pb–Sn and Pb–Sb alloy samples having similar coarse cell arrays are subjected to corrosion tests in order to assess the effect of Sn or Sb segregation in the cell boundary on the electrochemical performance. Electrochemical impedance spectroscopy (EIS) diagrams, potentiodynamic polarization curves and an equivalent circuit analysis are used to evaluate the electrochemical parameters in a 0.5 M H_2SO_4 solution at 25 °C. Both the experimental and simulated EIS parameters evidence different kinetics of corrosion. The Pb–1 wt.% Sn alloy is found to have a current density which is of about three times lower than that of the Pb–1 wt.% Sb alloy which indicates that dilute Pb–Sn alloys have higher potential for application as positive grid material in maintenance-free Pb-acid batteries.

1. Introduction

Due to the rapid development on lead-acid battery components for automotive applications in the past few decades, Pb–Sn, Pb–Sb, Pb–Ca–Sn and Pb–Ca–Sn–Sb alloys have been applied in the production of positive and negative grids, connectors, post and strap components of both VRLA and SLI batteries [1–4]. A battery grid must be dimensionally stable and have mechanical properties which can resist the stresses of the charge/discharge reactions without bending, stretching or warping. It is known that new additives have been sought for introduction in the grid alloy composition in order to improve its performance. In this context, rare earth elements, Ag, Te are added with the purpose of enhancing the alloy corrosion resistance, and to increase its creep resistance, thereby improving battery durability at high temperatures [4–16].

It is well known that the as-cast microstructure strongly influences the overall surface corrosion resistance of binary alloys [17–22]. It was found that the improvement on the corrosion resistance depends on the cooling rate imposed during solidification which affects the morphology and the scale of the microstructure and the solute redistribution (depending also on the electrochemical behavior of solute and solvent) [17–22].

The selection of appropriate levels of elements for the battery grids involves considerations of grid-production capability, economic feasibility, and metallurgical and electrochemical properties of the resulting alloys. Although different studies in the literature can be found [4–16] which focused on alloys of three or four alloying elements in the search for improvements in the grid performance, the present study aims to analyze the effect of combined metallurgical features of as-cast dilute Pb–Sn and Pb–Sb alloys. The effects of segregation of Sb or Sn to the cell boundaries in the resulting electrochemical corrosion behavior of as-cast Pb–1 wt.% Sn and Pb–1 wt.% Sb alloy samples in a 0.5 M H_2SO_4 solution at 25 °C was analyzed by parameterizing the scale of the cellular microstructure.

2. Experimental procedure

Pb–1 wt.% Sn and Pb–1 wt.% Sb alloys were prepared using commercially pure metals: Pb (99.89 wt.%), Sn (99.99 wt.%) and Sb (99.33 wt.%). The mean impurities were: Fe (0.12%), Si (0.05%), Cu (0.015%) and Fe (0.053%), Na (0.298%), Si (0.017%), Pb (0.247%), for Pb–Sn and Pb–Sb alloys, respectively, besides other elements with concentration less than 50 ppm.

A water-cooled unidirectional solidification designed in such way that the heat was extracted only through the water-cooled bottom, promoting vertical upward directional solidification was used in the experiments. More details concerning this solidification set-up and macrostructural/microstructural characterization can be obtained in previous articles [19,20]. As-cast Pb–Sn and Pb–Sb alloy samples were sectioned from the center of the ingot, ground, polished and etched to reveal the macrostructure, as shown in Fig. 1(a) and (b), respectively.

* Corresponding author. Tel.: +55 19 3521 3320; fax: +55 19 3289 3722.
E-mail address: wislei@fem.unicamp.br (W.R. Osório).

0378-7753/$ – see front matter © 2009 Elsevier B.V. All rights reserved.
doi:10.1016/j.jpowsour.2009.09.054

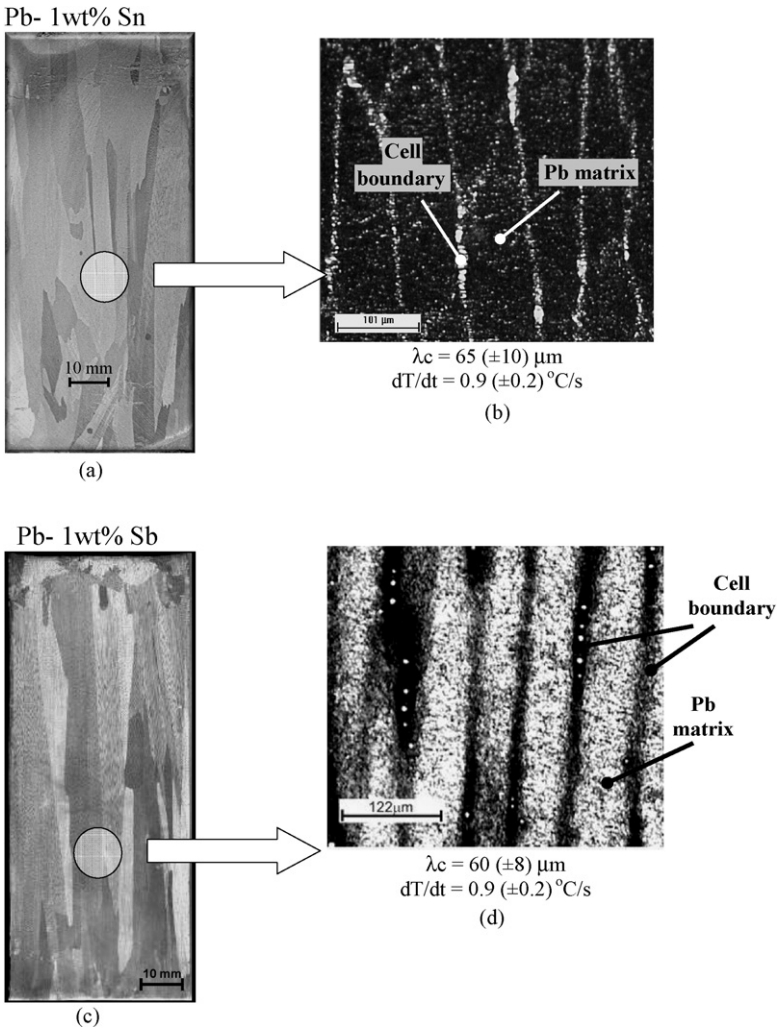

Fig. 1. ((a) and (c)) Typical directionally solidified macrostructure, and (b) and (d) typical cellular morphologies along the longitudinal sections at position 60 (±5 mm) from the bottom of the casting and its corresponding average cellular spacings and cooling rates for Pb–1 wt.% Sn and Pb–1 wt.% Sb alloys castings.

The electrochemical impedance spectroscopy (EIS) tests were carried out in a 0.5 M H_2SO_4 solution at 25 °C, using a similar procedure described in previous articles [19–22]. The potential amplitude was set to 10 mV, peak-to-peak (AC signal), with 5 points per decade and the frequency range was set from 100 mHz to 100 kHz in open circuit. The corrosion rate and corrosion potential were estimated by Tafel plots using both anodic and cathodic branches at a scan rate of 0.2 mV s^{-1} from −250/+250 mV (SCE). An appropriate model (ZView® version 2.1b) for equivalent circuit quantification has also been used.

3. Results and discussion

3.1. Macro- and microstructures

Fig. 1(a) and (c) depicts the resultant directionally solidified casting macrostructure for the Pb–1 wt.% Sn and Pb–1 wt.% Sb alloys castings, respectively. Due to the water-cooled unidirectional system, the growth of columnar grains has prevailed along the entire casting length, as also previously observed [19–21].

The samples for corrosion tests were collected at a midway position along the casting length as shown in a schematic representation in Fig. 1. Typical microstructures observed along longitudinal sections of both the Pb–1 wt.% Sn and Pb–1 wt.% Sb alloy castings are shown in Fig. 1(b) and (d). The as-cast microstructure of both alloys consists of complete cellular arrays, constituted by: (i) a Pb-rich matrix (α-phase: solid solution of tin in lead) with a eutectic mixture formation in the intercellular regions; and (ii) a Pb-rich matrix (α-phase: solid solution of antimony in lead) with a eutectic mixture formation in the intercellular regions. For the Pb–Sn alloy, the Pb-rich cellular matrix is depicted by dark regions with the intercellular eutectic mixture being represented by light regions, as shown in Fig. 1(b). For the Pb–Sb alloy, the Pb-rich matrix is represented by white regions with the intercellular region depicted by dark regions. In order to compare the resulting electrochemical corrosion behavior of these alloys samples with similar cell spacing were selected along the castings length in order to parameterize the scale of the cellular array. These samples had cell spacings of about 60–70 µm corresponding to distances from the casting cooled surface between 60 and 70 mm. As reported in previous articles [19–21], a water-cooled mold imposes higher values of cooling rates near the casting/chill surface (bottom) and a decreasing profile along the casting length (toward the top of the casting) due to the increase in the thermal resistance of the solidified shell with distance from the cooled surface.

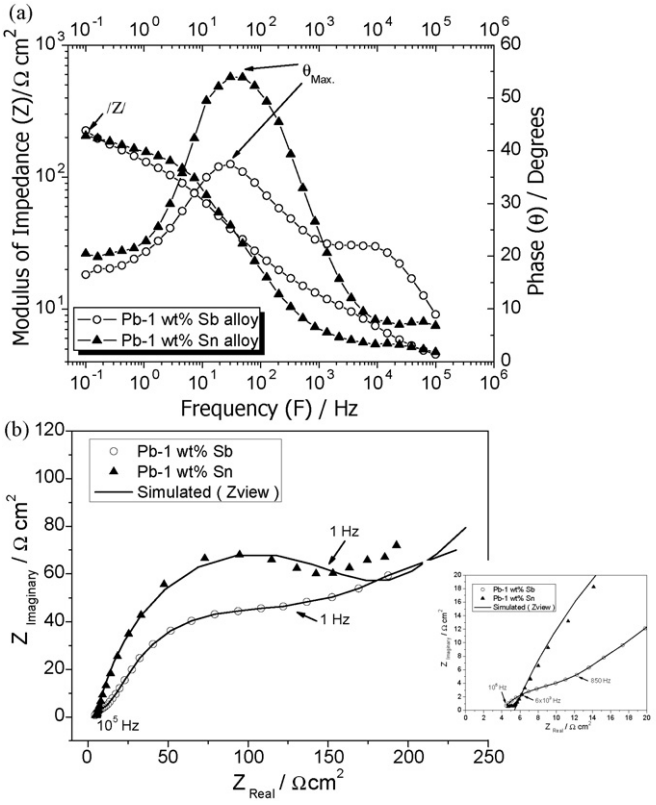

Fig. 2. (a) Experimental Bode and Bode-phase diagrams and (b) Nyquist plots (experimental and simulated: ZView®) for the Pb–1 wt.% Sn and Pb–1 wt.% Sb alloys in a 0.5 M H_2SO_4 solution at 25 °C.

3.2. Electrochemical corrosion behavior

Fig. 2 shows the Bode and Bode-phase diagrams representing the modulus of impedance and phase angle as a function of frequency. The Bode-phase results indicate that two time constants can be associated with the corrosion kinetics of the cellular array and the intercellular regions for both Pb–Sn and Pb–Sb alloys. For the Pb–Sb alloy, at a frequency range from 10^4 to 10^5 Hz, the first time constant, which can be related with the reaction between the electrolyte and the Sb-rich phase in the intercellular region, is clearly observed. At low frequencies, of about 27 Hz, the second time constant appears and can be correlated to the reaction between the electrolyte and the Pb-rich matrix. For the Pb–Sn alloy, a clear time constant is displayed at about 40 Hz and other time constant occurs at a frequency between 10^4 and 10^5 Hz. The maximum moduli of impedance (/Z/) of Pb–1 wt.% Sn and Pb–1 wt.% Sb alloys are similar (212 and 220 Ω cm²) at 0.1 Hz. At frequencies between 10 and 10^3 Hz, different slopes of /Z/ vs. F for the Pb–Sn and Pb–Sb alloys can be observed, which indicates that both the nature and

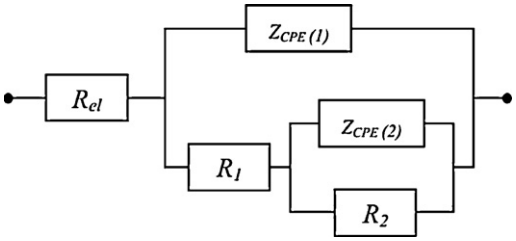

Fig. 3. Equivalent circuit used to obtain impedance parameters with the ZView® software.

Table 1
Impedance parameters obtained by the ZView® software fitting experimental and simulated results for Pb–1 wt.% Sn and Pb–1 wt.% Sb alloy samples in a 0.5 M H_2SO_4 solution at 25 °C.

Parameters	Pb–1 wt.% Sn	Pb–1 wt.% Sb
R_{el} (Ω cm²)	5.4	4.3
$Z_{CPE(1)}$ (μF cm^{-2})	360 (±36)	120 (±20)
$Z_{CPE(2)}$ (mF cm^{-2})	12 (±1)	1.8 (±1.3)
n_1	0.81	0.93
n_2	0.52	0.54
R_1 (Ω cm²)	170	30
R_2 (Ω cm²)	1500	300
χ^2	32×10^{-3}	25×10^{-3}

formation/evolution of the double layer are considerably different. Fig. 2(b) depicts the experimental

and simulated (ZView®) Nyquist plots of Pb–Sn and Pb–Sb alloy samples. Nyquist diagrams reveal capacitive arcs at high frequencies (between 10^5 and 1 Hz) followed by a slope of about 45° at frequencies lower than 1 Hz [23–25]. These Nyquist plots reveal that the diameters of the capacitive arcs for the Pb–Sn alloy are higher than those for the Pb–1 wt.% Sb alloy. These results show a similar tendency when compared to those analyzed in Bode and Bode-phase plots, shown in Fig. 2(a). These results indicate that the Pb–1 wt.% Sn alloy will be less corroded than the Pb–1 wt.% Sb alloy in a 0.5 M H_2SO_4 solution. At frequencies between 10^5 and 10^4 Hz, corresponding to 4.5–6 Ωcm² (Z_{real}), different reactions between

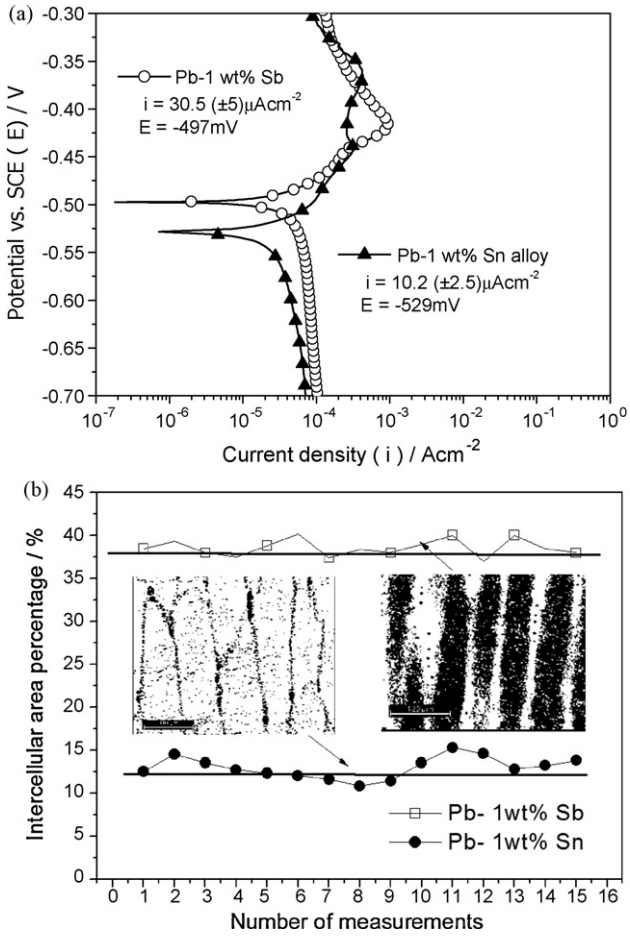

Fig. 4. (a) Experimental potentiodynamic polarization curves for Pb–1 wt.% Sb and Pb–1 wt.% Sn alloys in a 0.5 M H_2SO_4 solution at 25 °C and (b) Binary images representing typical intercellular area percentage of Pb–1 wt.% Sb (white regions) and Pb–1 wt.% Sn (black regions) alloys.

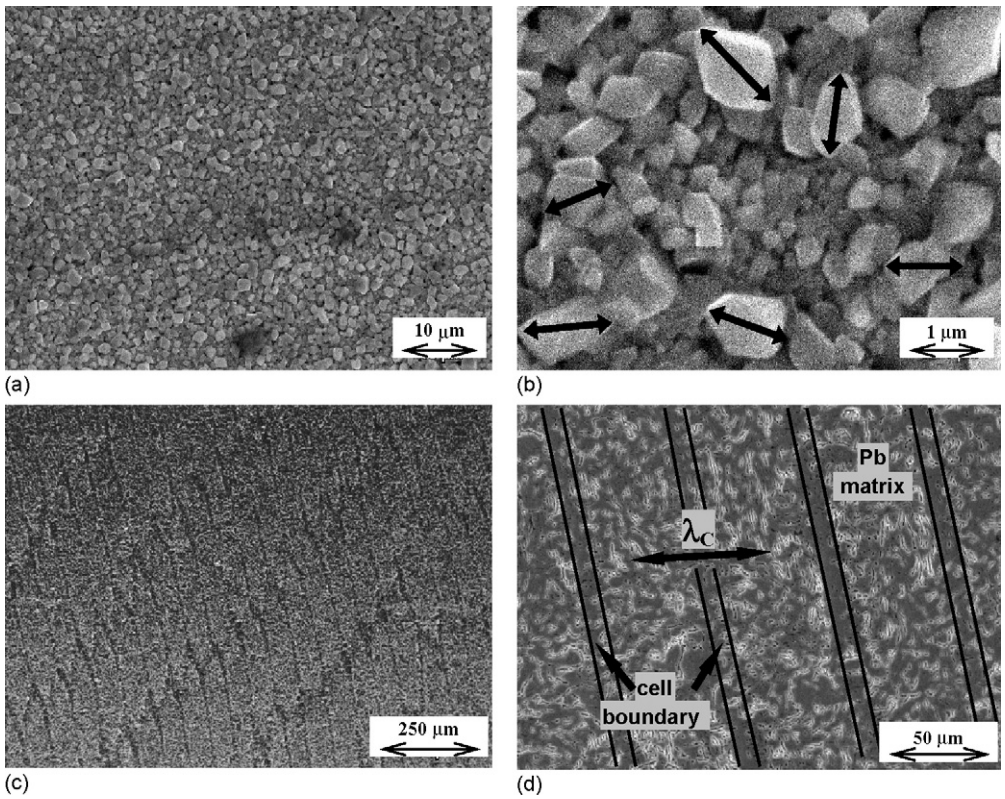

Fig. 5. Typical SEM images of a Pb–Sn alloy sample: (a) and (b) resulting corrosion product layer on a Pb–Sn alloy sample after EIS and potentiodynamic polarization tests in a 0.5 M H_2SO_4 solution at 25 °C, (c) and (d) after corrosion tests without corrosion product (removed with a 5% NaOH solution: immersion for 5 s) evidencing more severe corrosion action in the boundaries.

the electrolyte and the surface of the Pb–Sn and Pb–Sb alloy samples are expected to occur. These impedance parameters provide clear indication that the Pb–1 wt.% Sn alloy has an improved electrochemical behavior when compared with the Pb–1 wt.% Sb alloy.

An equivalent circuit analysis has also been conducted in order to obtain some impedance parameters [19–32]. The proposed equivalent circuit is shown in Fig. 3. The impedance parameters obtained by the ZView® software, are shown in Table 1. The fitting quality was evaluated by chi-squared (χ^2) values of 32×10^{-3} and 25×10^{-3} [28–32] for the Pb–1 wt.% Sn and Pb–1 wt.% Sb alloy samples, respectively. The interpretation of the physical elements of the proposed equivalent circuit is similar to those reported in previous studies [26–32]. It is observed that R_2 for both Pb–Sn and Pb–Sb alloys is about 10 times higher than R_1, which indicates that R_2 has an important role on the electrochemical corrosion resistance, as shown in Table 1. The impedance parameters, $Z_{CPE(2)}$ and R_2 closely correspond to those of adsorbed intermediates (e.g. $PbSO_4$, PbOH and other). $Z_{CPE(1)}$ corresponds to the double layer capacitance and R_1 corresponds to the polarization resistance at the surface of Pb alloys and high values also indicate lesser corrosion action.

Fig. 4(a) shows potentiodynamic polarization curves (from −0.7 to −0.3 V *vs.* SCE) for the Pb–1 wt.% Sn and Pb–1 wt.% Sb alloy samples in a 0.5 M H_2SO_4 solution at 25 °C. The corrosion current density (i_{corr}) was obtained from Tafel plots using both the cathodic and anodic branches of the polarization curves [17–22].

The experimental corrosion potentials which resulted from corrosion tests carried out in open circuit in a 0.5 M H_2SO_4 solution after achieving a steady-state condition were: −650 (SCE), −550 (SCE) and −350 mV (SCE) for commercially pure samples of tin (Sn), lead (Pb), and antimony (Sb), respectively [19,20]. A nobler potential is evidenced by pure Sb samples when compared to Sn samples which can be associated with the observed displacement of about 30 mV (SCE) in the corrosion potential of the Pb–Sb alloys, as shown in Fig. 4. However, it seems that an improvement of galvanic protection is provided by the eutectic mixture of the Pb–Sn alloy (variation of potential: ±100 mV, SCE) when compared to the Pb–Sb alloy (variation of potential: ±200 mV, SCE) alloy. These considerations are reinforced when current density results are considered. A current density of about 10 (±2.5) $\mu A \times cm^{-2}$ associated with a corrosion potential of about −529 mV (SCE) was observed for the Pb–Sn alloy sample. Although the Pb–1 wt.% Sb alloy sample has a corrosion potential displaced (of about 30 mV *vs.* SCE) toward the more positive potential, its corresponding current density is about three times higher (of about 30 (±5) $\mu A \times cm^{-2}$) than that of the Pb–Sn alloy. It is important to remark that both the Pb–Sn and Pb–Sb alloy samples were selected at positions along the casting length corresponding to cell spacing between 60 and 70 μm.

At potentials between −520 and −490 mV (SCE), anodic oxidation of Pb can take place and the prediction of corrosion kinetics by the formation of $Pb/PbO/PbSO_4$ and Pb/PbO_2 electrode systems can be made. Description and discussion of such phenomena have been previously reported in the literature [21,22,33–35].

It is known that during solidification of Pb–Sn and Pb–Sb alloys, tin and antimony are segregated, respectively, toward the grain boundaries [19–22]. For cellular structures, galvanic cells are formed in the eutectic mixture at the cell boundaries. Previous studies [19–22] reported that the cell boundaries are regions of higher energy which is a result of distortions at the limits between adjacent cells during growth along the solidification process. Considering the intercellular area percentage (IAP) which represent the regions more electrochemically active of both the Pb–Sn and Pb–Sb alloy samples, it can be seen that the Pb–Sb alloy has an IAP of about three times higher (38%: white region) than the Pb–Sn alloy (12%: black region), as shown in Fig. 4(b). These IAP averages have been determined using the ImageJ® software analyzing binary images [36]. It can also be seen that, despite the similar cellular spacings

considered for Pb–Sb and Pb–Sn alloy samples, their corresponding intercellular average widths were 24 and 8 μm, respectively.

The present experimental observations permit to conclude that the resulting microstructural morphology has an important role on the electrochemical behavior of the dilute Pb–Sn and Pb–Sb alloys examined. Thus, independently of the electrochemical characteristic of the solute segregated in the cell boundaries, the cell spacing associated with the intercellular boundaries (active regions) will determine the corrosion susceptibility of dilute Pb alloys.

It is important to remark that the alloy solute content can considerably modify the electrochemical behavior of these alloys. In particular for Pb–Sb alloys in the range of compositions normally used in the manufacture of battery components, it was shown that cellular microstructures prevail for concentrations less than 3 wt.% Sb, and dendritic arrangements are associated with alloy concentrations which are higher than 3 wt.% Sb. Furthermore, coarse cellular structures have proved to be more corrosion resistant than fine cellular arrays. The opposite has been observed for dendritic microstructures with finer structural arrangements providing higher corrosion resistance [19]. It has been suggested that casting processes associated with low cooling rates would be more appropriate for the manufacture of low Sb alloys grids (due to the resulting coarse cell morphology) while Pb–Sb battery components having compositions which are higher than 3 wt.% Sb should be cast under conditions of high cooling rates (due to the resulting finer dendritic spacings) [19].

After EIS and potentiodynamic polarization tests in a 0.5 M H_2SO_4 solution at 25 °C, some selected samples of Pb–Sn and Pb–Sb alloys were carefully washed in distilled water, air dried, and subsequently subjected to SEM analyses. Fig. 5(a) and (b) shows typical SEM images of a Pb–Sn alloy sample depicting particles of the corrosion product. These particles seem to be consisted by two levels of particle sizes: (i) between 0.2 and 1 μm and (ii) between 1 and 2 μm. It seems that these particles are directly associated with the measured $Z_{CPE(1)}$ and $Z_{CPE(2)}$ parameters corresponding to porous and barrier layers, respectively [27–33]. Fig. 5(b) depicts some selected particles (arrows) having sizes from 1 to 2 μm. Fig. 5(c) and (d) shows SEM images after EIS and potentiodynamic tests in a 0.5 M H_2SO_4 solution without corrosion product layer which was removed by a 5% NaOH solution at room temperature. It can be observed a more severe corrosion action in the boundaries, although some corroded areas can also be seen at the Pb-rich phase (Pb cell matrix).

Lead-acid battery manufacturers are constantly engaged in the search of improvements in production features with a view to decrease battery grid weight as well as to reduce the production costs [1–4]. Considering a conventional manufacture of lead-acid battery components, the use of either a Pb–1 wt.% Sb alloy or a Pb–1 wt.% Sn alloys will result in a similar final battery weight, metallurgical aspects and production costs. However, dilute Pb–Sn alloys will be less corroded when compared with the Pb–Sb alloy. This indicates that the control of solidification processing variables (e.g. cooling rate) of this alloy can be used as an alternative way to produce as-cast lead-acid battery components having higher corrosion resistance.

4. Conclusions

The present experimental electrochemical parameters indicate that a dilute Pb–1 wt.% Sn alloy tends to yield higher corrosion resistance than a dilute Pb–1 wt.% Sb alloy when similar cellular arrays are considered. It was found that better galvanic protection is provided by the eutectic mixture of the Pb–Sn alloy when compared to the Pb–Sb alloy. A current density of about three times higher ($30 \pm 5\ \mu A \times cm^{-2}$) was attained by the Pb–Sb alloy when compared to that of the Pb–Sn alloy ($10 \pm 2.5\ \mu A \times cm^{-2}$). The EIS experimental parameters obtained using the ZView® software have also supported this conclusion. It can be said that independently of the electrochemical characteristic of the solute segregated in the cell boundaries, the cell spacing associated with the intercellular boundaries (active regions) will determine the corrosion susceptibility of the dilute Pb alloy. In this context, the manufacturers of as-cast components should consider the control of solidification processing variables (e.g. cooling rate) of dilute Pb–Sn alloys as an alternative way to produce lead-acid battery components with better electrochemical behavior. Obviously, a number of other Pb alloy systems can be considered for the production of Pb-acid battery components by introducing a third or fourth alloying element. However, these procedures can introduce a higher level of difficulty for the simultaneous control of the final chemical composition and the resulting microstructures which have important roles on the final electrochemical corrosion resistance.

Acknowledgements

The authors acknowledge financial support provided by FAPESP (The Scientific Research Foundation of the State of São Paulo, Brazil), FAEPEX-UNICAMP, and CNPq (The Brazilian Research Council).

References

[1] M.D. Achtermann, M.E. Greenlee, J. Power Sources 33 (1991) 87–92.
[2] J. Wirtz, Batteries Int. (1996) 56, January.
[3] R.D. Prengaman, J. Power Sources 95 (2001) 224–233.
[4] R.D. Prengaman, in: K.R. Bullock, D. Pavlov (Eds.), Proceedings vol. 84-14 Advances in Lead-acid Batteries, The Electrochemical Society, Pennington, NJ, 1984, p. 201.
[5] R.D. Prengaman, J. Power Sources 158 (2006) 1110–1116.
[6] G.S. Al-Ganainy, M.T. Mostafa, F. Abd El-Salam, Physica B 348 (2004) 242–248.
[7] B. Rezaei, S. Damiri, J. Solid State Electrochem. 9 (2005) 590–594.
[8] J. Furukawa, Y. Nehyo, S. Shiga, J. Power Sources 133 (2004) 25–31.
[9] W.X. Guo, D. Shu, H.Y. Chen, A.J. Li, H. Wang, G.M. Xiao, C.L. Dou, S.G. Peng, W.W. Wei, W. Zhang, H.W. Zhou, S. Chen, J. Alloys Compd. 475 (2009) 102–109.
[10] H.T. Liu, J. Yang, H.H. Liang, J.H. Zhuang, W.F. Zhou, J. Power Sources 93 (2001) 230–233.
[11] Y.B. Zhou, C.X. Yang, W.F. Zhou, H.T. Liu, J. Alloys Compd. 365 (2004) 108–111.
[12] M. Shiota, T. Kameda, K. Matsui, N. Hirai, T. Tanaka, J. Power Sources 144 (2005) 358–364.
[13] T. Hirasawa, K. Sasaki, M. Taguchi, H. Kaneko, J. Power Sources 85 (2000) 44–48.
[14] C.S. Lakshmi, J.E. Manders, D.M. Rice, J. Power Sources 73 (1998) 23–29.
[15] S. Stein, G. Bourguinon, L. Raboin, L. Broch, L. Johann, E. Rocca, Thin Solid Films 455–456 (2004) 735–741.
[16] E. Rocca, J. Steinmetz, Electrochim. Acta 44 (1999) 4611–4618.
[17] W.R. Osório, C.S.C. Aoki, A. Garcia, Mater. Sci. Forum 595–598 (2008) 851–859.
[18] W.R. Osório, P.R. Goulart, G.A. Santos, C. Moura Neto, A. Garcia, Metall. Mater. Trans. A 37 (2006) 2525–2537.
[19] W.R. Osório, D.M. Rosa, A. Garcia, J. Power Sources 175 (2008) 595–603.
[20] D.M. Rosa, J.E. Spinelli, W.R. Osório, A. Garcia, J. Power Sources 162 (2006) 696–705.
[21] W.R. Osório, C. Aoki, A. Garcia, J. Power Sources 185 (2008) 1471–1477.
[22] L.C. Peixoto, W.R. Osório, A. Garcia, J. Power Sources 192 (2009) 724–729.
[23] W.J. Lorenz, F. Mansfeld, Corros. Sci. 21 (1981) 647–672.
[24] W.R. Osório, L.C. Peixoto, L.R. Garcia, A. Garcia, Acta Met. Sin. 22 (2009) 241–246.
[25] A. Li, Y. Cheni, H. Chen, D. Shu, W. Li, H. Wang, C. Dou, W. Zhang, S. Chen, J. Power Sources 189 (2009) 1204–1211.
[26] F. Mansfeld, M.W. Kendig, J. Electrochem. Soc. 135 (1998) 828–835.
[27] J. Pan, D. Thierry, C. Leygraf, Electrochim. Acta 41 (1996) 1143–1153.
[28] S. Gudic, J. Radosevic, M. Kliskic, Electrochim. Acta 47 (2002) 3009–3016.
[29] S.L. Assis, S. Wolynec, I. Costa, Electrochim. Acta 51 (2006) 1815–1819.
[30] W.R. Osório, P.R. Goulart, A. Garcia, Mater. Lett. 62 (2008) 365–369.
[31] A. Cremasco, W.R. Osório, C.M.A. Freire, A. Garcia, R. Caram, Electrochim. Acta 53 (2008) 4867–4875.
[32] W.R. Osório, L.C. Peixoto, A. Garcia, Mater. Corros., in press, doi:10.1002/maco.200805181.
[33] D. Pavlov, M. Bojinov, T. Laitinen, G. Sundholm, Electrochim. Acta 36 (1991) 2087–2092.
[34] D. Pavlov, M. Bojinov, T. Laitinen, G. Sundholm, Electrochim. Acta 36 (1991) 2081–2086.
[35] D. Pavlov, B. Monahov, G. Sundholm, T. Laitinen, J. Electroanal. Chem. 305 (1991) 57–63.
[36] L.R. Garcia, W.R. Osório, L.C. Peixoto, A. Garcia, J. Electron. Mater. 38 (2009) 2405–2414.